

See discussions, stats, and author profiles for this publication at: <https://www.researchgate.net/publication/280243450>

Fluorine-Doped SnO₂@Graphene Porous Composite for High Capacity Lithium-Ion Batteries

ARTICLE *in* CHEMISTRY OF MATERIALS · JUNE 2015

Impact Factor: 8.35 · DOI: 10.1021/acs.chemmater.5b00885

CITATIONS

3

READS

67

1 AUTHOR:



Jianxin Geng

Technical Institute of Physics and Chemistry

54 PUBLICATIONS 1,380 CITATIONS

SEE PROFILE

Fluorine-Doped SnO₂@Graphene Porous Composite for High Capacity Lithium-Ion Batteries

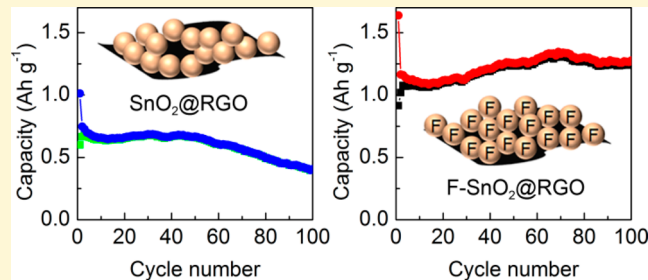
Jinhua Sun,^{†,‡} Linhong Xiao,[†] Shidong Jiang,[†] Guoxing Li,[†] Yong Huang,[†] and Jianxin Geng^{*,†}

[†]Technical Institute of Physics and Chemistry, Chinese Academy of Sciences, 29 Zhongguancun East Road, Haidian District, Beijing 100190, China

[‡]University of Chinese Academy of Sciences, 19A Yuquan Road, Beijing 100049, China

Supporting Information

ABSTRACT: For the first time, a composite of fluorine-doped SnO₂ and reduced graphene oxide (F-SnO₂@RGO) was synthesized using a cheap F-containing Sn source, Sn(BF₄)₂, through a hydrothermal process. X-ray photoelectron spectroscopy and X-ray diffraction results identified that F was doped in the unit cells of the SnO₂ nanocrystals, instead of only on the surfaces of the nanoparticles. F doping of SnO₂ led to more uniform and higher loading of the F-SnO₂ nanoparticles on the surfaces of RGO sheets, as well as enhanced electron transportation and Li ion diffusion in the composite. As a result, the F-SnO₂@RGO composite exhibited a remarkably high specific capacity (1277 mA h g⁻¹ after 100 cycles), a long-term cycling stability, and excellent high-rate capacity at large charge/discharge current densities as anode material for lithium ion batteries. The outstanding performance of the F-SnO₂@RGO composite electrode could be ascribed to the combined features of the composite electrode that dealt with both the electrode dynamics (enhanced electron transportation and Li ion diffusion due to F doping) and the electrode structure (uniform decoration of the F-SnO₂ nanoparticles on the surfaces of RGO sheets and the three-dimensional porous structures of the F-SnO₂@RGO composite).



INTRODUCTION

In recent years, tin dioxide (SnO₂) as an anode material for lithium-ion batteries (LIBs) has attracted enormous attention among scientists due to its high theoretical capacity (ca. 1494 mA h g⁻¹),^{1,2} which is much higher than the value of the commercialized anode material graphite (372 mA h g⁻¹). However, the practical use of SnO₂ as anode material for LIBs has been handicapped by huge volume changes (up to 260%)⁵ and serious aggregation of tin particles during the lithiation/delithiation process, leading to stress-induced pulverization of the electrode and severe capacity fading of the resultant LIB cells.⁶ Extensive studies, including rational design of hierarchical hollow or mesoporous structures using SnO₂ building blocks^{7,8} and integration of the electrode materials with carbonaceous matrix,^{4,9–11} have been performed to overcome the limitations of pristine SnO₂ as anode material for LIBs. Lou's group has conducted a series of pioneering researches on SnO₂ based LIBs through controlling the morphologies of SnO₂^{12,13} and fabricating hybrid structures with carbon materials.^{14–16} Nevertheless, the performance of the SnO₂-based anode materials, especially their poor long-term cycling stability at large charge/discharge current density, is still not satisfactory for commercialization.

Alternative effort to improve the electrochemical performance of SnO₂ as anode material for LIBs was directed to doping SnO₂ or the SnO₂/graphene composites with exotic atoms.

Several studies focused on the composites of nitrogen-doped reduced graphene oxide (N-RGO) and SnO₂,^{3,17–19} in which the formed Sn–N–C bond resulted in homogeneous loading of SnO₂ nanoparticles on the surfaces of the N-RGO sheets, and thereafter prevented the Sn nanoparticles from agglomerating during the lithiation/delithiation process.¹⁸ Incorporation of heterocation such as Sb⁵⁺ or Zn²⁺ into SnO₂ efficiently enhanced the electrical conductivity and facilitated the Li ion diffusion in the resultant SnO₂-based electrodes, leading to enhanced capacity and cycling performance compared with the nondoped counterpart.^{20,21} Fluorine, as an important anion dopant, substitute the O²⁻ in SnO₂ to yield a high electrical conductivity (up to 1×10^3 S cm⁻¹)²² compared with the pristine SnO₂ (with a band gap energy $E_g = 3.62$ eV at 300 K).²⁰ Additionally, F doped materials were reported to exhibit enhanced thermal stability and good corrosion resistant properties.^{23–26} As a result, F-doped SnO₂ (F-SnO₂) has been widely used in multidiscipline researches such as transparent conductive material.²⁷ However, the effect of F doping on the performance of SnO₂-based anode materials for LIBs has not been well studied.²⁸ Capitalizing on the unique features of F doping, we expect that F doping of SnO₂ may

Received: March 8, 2015

Revised: June 13, 2015

Published: June 16, 2015



open up a new approach to address the issues associated with SnO₂-based anode materials for LIBs.

Here, to investigate the effect of F doping on the performance of SnO₂ based materials as anode for LIBs, we *in situ* synthesized three-dimensional (3D) porous composite of F-SnO₂ and RGO (F-SnO₂@RGO) through a one-step hydrothermal method using a F-containing Sn source, Sn(BF₄)₂. F doping results in stronger interactions between F-SnO₂ and RGO sheets, leading to more uniform and higher loading of F-SnO₂ nanoparticles on RGO sheets. What is most important is that F doping could decrease the charge transfer resistance of the resultant F-SnO₂@RGO electrode. Therefore, the F-SnO₂@RGO electrode not only allows fast access of electrolyte into the 3D porous structure and improves electron transportation and Li ion diffusion in the electrode, but also exhibits elongated cycling stability due to the corrosion resistant effect of the F doped electrode material.^{23–25} As a result, the LIB cells prepared using the F-SnO₂@RGO composite as anode material exhibit outstanding performance such as high specific capacity (1277 mA h g⁻¹ after 100 cycles), excellent rate capacity at high charge/discharge current densities, and elongated cycling stability.

■ EXPERIMENTAL SECTION

Preparation of Graphene Oxide (GO) Hydrogel. GO was synthesized from natural graphite powders by a modified Hummer's method.^{29,30} The GO was thoroughly purified by cycles of washing with deionized (DI) water and centrifuging. GO hydrogel was finally obtained by decanting the supernatant. The concentration of the GO hydrogel was determined by drying a portion of the as-prepared GO hydrogel at 50 °C overnight in a vacuum oven. A GO suspension (3 mg mL⁻¹) was prepared by dispersing the GO hydrogel in DI water.

Synthesis of the F-SnO₂@RGO Composite. In a typical reaction, the GO suspension (3 mg mL⁻¹, 10 mL), a Sn(BF₄)₂ solution (50 wt % in H₂O, 0.5 mL), and ethylenediamine (EDA) (90 µL) were added to a 30 mL Teflon-lined autoclave under stirring. The hydrothermal reaction was allowed to take place at 180 °C for 24 h. After cooling, the black product was thoroughly washed with DI water and freeze-dried. Finally, the obtained sample was thermally treated at 400 °C for 2 h in a tube furnace under the atmosphere of Ar. To synthesize composites with different contents of F-SnO₂ nanoparticles, we used various amounts of Sn(BF₄)₂ solution in the hydrothermal reaction.

Synthesis of the SnO₂@RGO Composite. The SnO₂@RGO was obtained by following the same procedure as for F-SnO₂@RGO, but a SnCl₂·2H₂O solution (75 mg of SnCl₂·2H₂O in 10 mL of DI water) was used as a Sn precursor. To synthesize composites with different contents of SnO₂ nanoparticles, we used various amounts of SnCl₂·2H₂O solution in the hydrothermal reaction.

Synthesis of RGO. RGO was prepared by following the same procedure as preparing the F-SnO₂@RGO, but no Sn sources were used.

Characterization. The X-ray diffraction (XRD) patterns were collected on a Bruker D8 Focus diffractometer with an incident wavelength of 0.154 nm (Cu K α radiation) and a Lynx-Eye detector. Thermogravimetric analysis (TGA) measurement was carried out with a TGA Q50 at a scanning rate of 10 °C min⁻¹. X-ray photoelectron spectra (XPS) were recorded on a PHI Quantera Scanning X-ray Microprobe with a monochromated Al K α radiation of 1486.7 eV. N₂ adsorption-desorption isotherms and pore-size distribution were obtained on a QuadraSorb SI MP apparatus at 77 K. Raman spectra were recorded on a Renishaw inVia-Reflex confocal Raman microscope with an excitation wavelength of 532 nm. Scanning electron microscope (SEM) observations were performed on a field-emission SEM (Hitachi S-4800) equipped with an energy-dispersive X-ray spectroscopy (EDS). Transmission electron microscope (TEM) images were obtained using a JEOL-2100F microscope operated under an accelerating voltage of 200 kV.

Electrochemical Measurement. Electrochemical performance of F-SnO₂@RGO and SnO₂@RGO composites, as well as F-SnO₂ and SnO₂ nanoparticles without RGO, was measured in CR 2032-type coin cells. Working electrodes were fabricated by mixing the electrode materials, Super P carbon black, and poly(vinylidene fluoride) binder in *N*-methyl pyrrolidone with a weight ratio of 80:10:10. The obtained slurry was uniformly pasted on a copper foil and dried at 120 °C in a vacuum oven overnight. Pure lithium metal foil was used as the counter electrode and a LiPF₆ solution (1 M) in a mixture of ethylene carbonate and diethyl carbonate (1:1 by volume) was used as the electrolyte. The cells were assembled in an Ar-filled glovebox. Cyclic voltammetry (CV) curves were collected on a Zennium 40088 electrochemical workstation at a scan rate of 0.1 mV s⁻¹. Electrochemical impedance spectra (EIS) were also recorded on the Zennium 40088 electrochemical workstation by applying a sine wave with amplitude of 10 mV over a frequency range from 100 kHz to 10 mHz. The charge/discharge cycling tests were galvanostatically performed between 0.005 and 3 V (vs Li/Li⁺) at room temperature.

■ RESULTS AND DISCUSSION

F-SnO₂ nanocrystals were successfully prepared by oxidation of a cheap F-containing Sn²⁺ complex Sn(BF₄)₂ as the single source of Sn and F. Figure 1 illustrates that the F-SnO₂@RGO

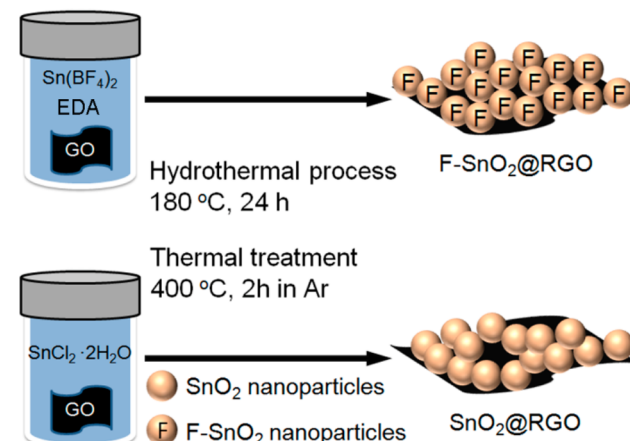


Figure 1. Schematic illustration of synthesizing the F-SnO₂@RGO and SnO₂@RGO composites.

was synthesized through an *in situ* hydrothermal method with the aid of EDA and in the presence of GO. The use of EDA was intended to reduce the size of the F-SnO₂ nanoparticles down to nanometer scale because EDA functioned as a structure-direction template and assisted the anisotropic crystal growth of inorganic nanoparticles.^{31,32} During the hydrothermal process, the GO was partially reduced into RGO because of the thermal cleavage of the oxygen-containing groups;³³ meanwhile the RGO assembled into a 3D porous structure. Because of the bonding between metal oxides and RGO sheets,^{18,34,35} the F-SnO₂ nanoparticles can be uniformly anchored on the surfaces of RGO sheets to form F-SnO₂@RGO composite. In control, a nondoped counterpart, SnO₂@RGO, was also synthesized through a similar manner by using SnCl₂·2H₂O as Sn source. Finally, both F-SnO₂@RGO and SnO₂@RGO composites were thermally annealed to enhance the crystallinity of the F-SnO₂ and SnO₂ nanoparticles and the reduction degree of the RGO.

The crystal structure of the F-SnO₂@RGO composite was characterized using XRD. All the Bragg reflection peaks of the F-SnO₂@RGO composite can be indexed according to tetragonal SnO₂ with P42/mnm (136) space groups (JCPDS NO.41-1445) (Figure 2a), indicating that the F-SnO₂

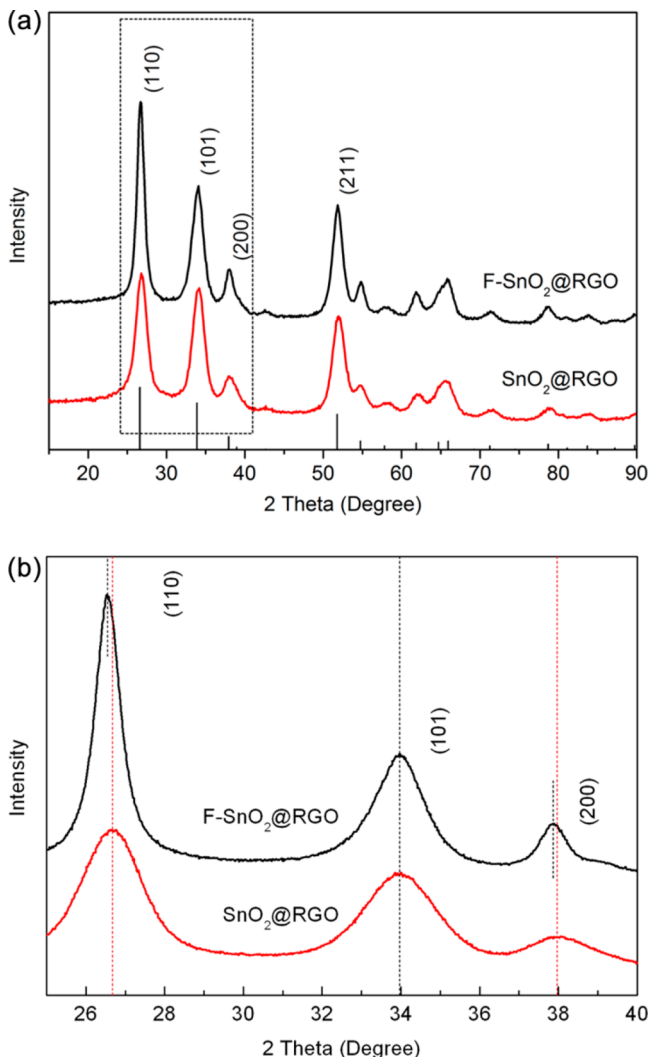


Figure 2. (a) Comparison of the XRD patterns of the F-SnO₂@RGO and SnO₂@RGO composites and the standard XRD pattern of SnO₂, showing that the F-SnO₂ has the same crystal structure as SnO₂. (b) Extended XRD patterns of the F-SnO₂@RGO and SnO₂@RGO composites, showing that (110) and (200) reflections of the F-SnO₂ shifted to lower angles.

possesses a pure crystalline phase. Close investigation revealed that the (110) and (200) reflections of the F-SnO₂ slightly shifted to lower angles compared with that of the SnO₂: from 26.68 to 26.56° for (110) reflection and from 38.01 to 37.87° for (200) reflection (Figure 2b). From the analysis of the XRD pattern, the lattice parameters (*a*, *b*, and *c*) of the tetragonal cell were obtained: the lattice parameters *a* and *b* of the F-SnO₂ (*a* = *b* = 4.743(3) Å) became larger than that of the SnO₂ (*a* = *b* = 4.714(5) Å), whereas the lattice parameter *c* showed negligible change (*c* = 3.167(1) Å for F-SnO₂ and *c* = 3.169(1) Å for SnO₂). The swelling of the unit cells could be due to the replacement of smaller O²⁻ (ionic radius 0.132 nm) by larger F⁻ (ionic radius 0.133 nm) in the SnO₂ cells.³⁶ In addition, the average grain size of the F-SnO₂ crystallites estimated from the (110) Bragg reflection is ca. 9.5 nm according to Scherrer's equation, and the average grain size of the SnO₂ crystallites is ca. 8.0 nm.

XPS was used to further prove the incorporation of F into the F-SnO₂@RGO composite. The survey XPS curve indicated that F was present in the F-SnO₂@RGO composite with a

content of 3.5 atom % (Figure 3a). Figure 3b displays the Sn 3d XPS curves of the F-SnO₂@RGO and SnO₂@RGO compo-

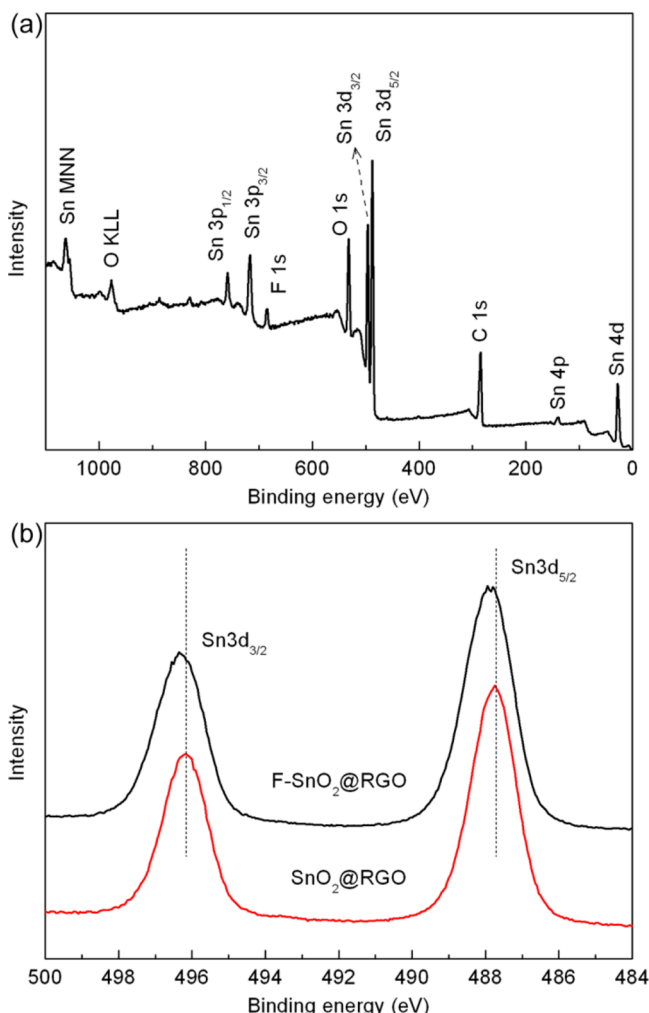


Figure 3. (a) Survey XPS curve of the F-SnO₂@RGO composite, showing the presence of F in the composite. (b) Comparison of the high-resolution Sn 3d XPS curves of the F-SnO₂@RGO and SnO₂@RGO composites, showing that the binding energies corresponding to Sn 3d_{5/2} and Sn 3d_{3/2} for the F-SnO₂ shifted to higher binding energy levels compared with that of SnO₂.

sites. The distance between the binding energies corresponding to Sn 3d_{5/2} and Sn 3d_{3/2} was 8.4 eV for the F-SnO₂, which was in good agreement with the energy splitting reported for SnO₂.³⁷ But, the binding energies corresponding to Sn 3d_{5/2} and Sn 3d_{3/2} for the F-SnO₂ shifted to higher levels compared with that of SnO₂, indicating a decreased electron density in the 3d orbital of Sn due to the substitution of O²⁻ by more electronegative F⁻ in SnO₂ cells.^{24,38} Considering the evidence from both XRD and XPS results, we conclude that the F has been doped in the unit cells of SnO₂, instead of only on the surfaces of the nanoparticles. On the other hand, although a peak corresponding to the C–F species was found at 289.8 eV in the C 1s XPS curve of the F-SnO₂@RGO composite, the peak was so weak that F doping of RGO was negligible (Figure S1 in the Supporting Information).

The morphology and microstructure of the F-SnO₂@RGO composite were characterized by SEM, TEM, and N₂ physisorption measurements. The SEM image shows that the

F-SnO₂@RGO composite contained 3D architecture with porous structures in the range of nanometer to micrometer scale (Figure 4a). A folded individual sheet reveals that the F-

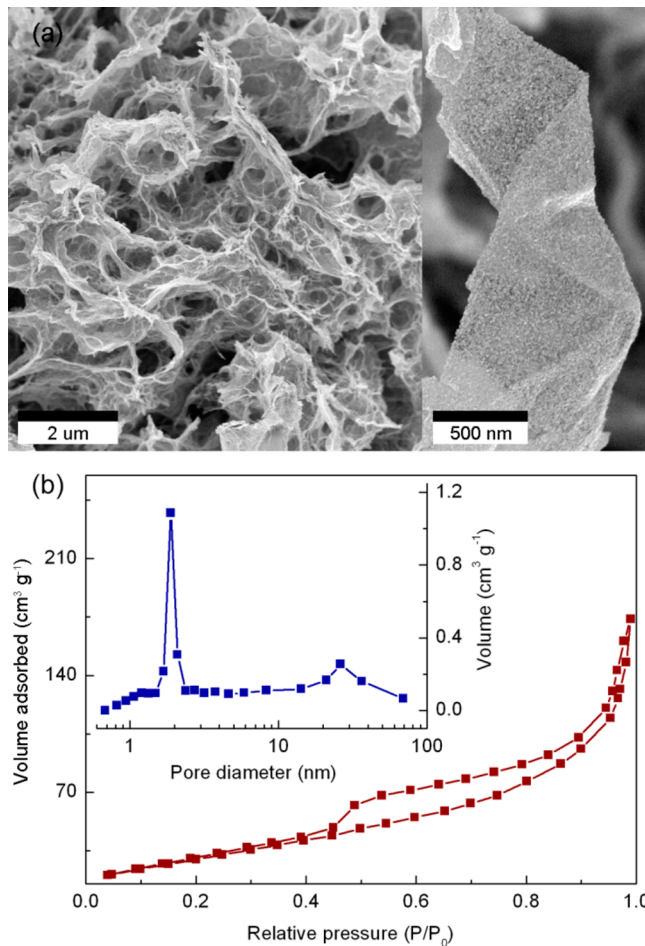


Figure 4. (a) SEM image of the F-SnO₂@RGO composite, showing the 3D porous structures in the composite. Inset: A folded individual composite sheet, showing that the F-SnO₂ nanoparticles were uniformly decorated on the two sides of the RGO sheet. (b) N₂ adsorption/desorption isotherms of the F-SnO₂@RGO composite and the pore-size distribution plot shown in the inset.

SnO₂ nanoparticles are uniformly decorated on the two sides of the RGO sheet (inset of Figure 4a). In addition, the uniform distribution of F element throughout the F-SnO₂@RGO composite is proved using EDS (Figure S2 in the Supporting Information). In the N₂ adsorption–desorption isotherms (Figure 4b), the F-SnO₂@RGO composite exhibits a gradually increasing adsorption at a low relative pressure (P/P_0) and a high adsorption uptake at a high P/P_0 (i.e., as the P/P_0 approaching to 1), being indicative of the existence of plenty of macropores. In addition, a hysteresis loop can be seen within a P/P_0 from 0.4 to 0.9 in the desorption isotherm, implying existence of mesopores. The inset shows that the pore size distributes in the range of 2–70 nm, along with the larger open pores observed from SEM image (Figure 4a). The specific surface area read from the desorption data is ca. 129 m² g⁻¹, which is lower than that of pure RGO because of the decoration of the F-SnO₂ nanoparticles.³⁹ For comparison, the SnO₂@RGO composite was also characterized with SEM, EDS mapping, and N₂ physisorption measurement (Figures S3 and

S4 in the Supporting Information). The structural parameters of the F-SnO₂@RGO and SnO₂@RGO composites are summarized in Table S1 in the Supporting Information. One can see that the F-SnO₂@RGO and SnO₂@RGO composites have very similar structural parameters, getting rid of the impact of structural characteristics on the electrochemical performances of the two composites for LIBs. The high specific surface area and the 3D porous architecture of the F-SnO₂@RGO composite not only facilitate the access of electrolyte, but also accommodate the volume changes of the composite electrode during lithiation/delithiation process when used as anode material in LIBs.

Figure 5a and 5c display typical TEM images of the F-SnO₂@RGO and SnO₂@RGO composites. Although some F-

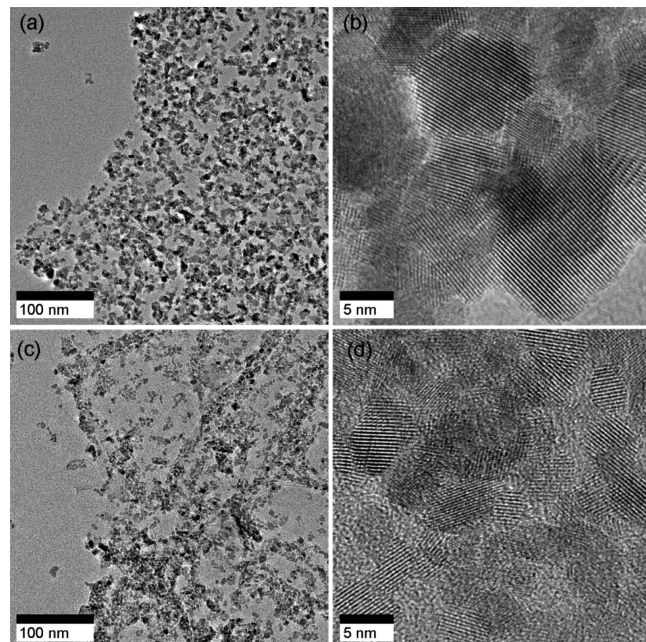


Figure 5. (a, b) TEM and HRTEM images of the F-SnO₂@RGO composite. (c, d) TEM and HRTEM images of the SnO₂@RGO composite. The TEM data indicate that the F-SnO₂ nanoparticles are more uniformly attached on the surfaces of RGO sheets than the SnO₂ nanoparticles.

SnO₂ nanoparticles can be found to connect with each other, aggregation of the nanoparticles has been markedly alleviated compared with the SnO₂ nanoparticles in the SnO₂@RGO composite. TGA data indicated that the F-SnO₂ accounted for 82 wt % in the F-SnO₂@RGO composite and the SnO₂ accounted for 75 wt % in the SnO₂@RGO composite (Figure S5 in the Supporting Information). F-SnO₂@RGO and SnO₂@RGO composites with higher contents of the respective nanoparticles were also synthesized, but TEM observations indicate that plenty of detached F-SnO₂ and SnO₂ nanoparticles exist in the respective composites (Figures S6 and S7 in the Supporting Information). Because the detached SnO₂ nanoparticles are not beneficial to good performance of the composites as anode material for LIBs,^{17,18} the F-SnO₂@RGO with 82 wt % F-SnO₂ and the SnO₂@RGO with 75 wt % SnO₂ were used for further characterization and preparation of LIB cells. Furthermore, the higher loading and more uniform distribution of the F-SnO₂ nanoparticles on the RGO sheets might be due to more intimate interactions between the F-

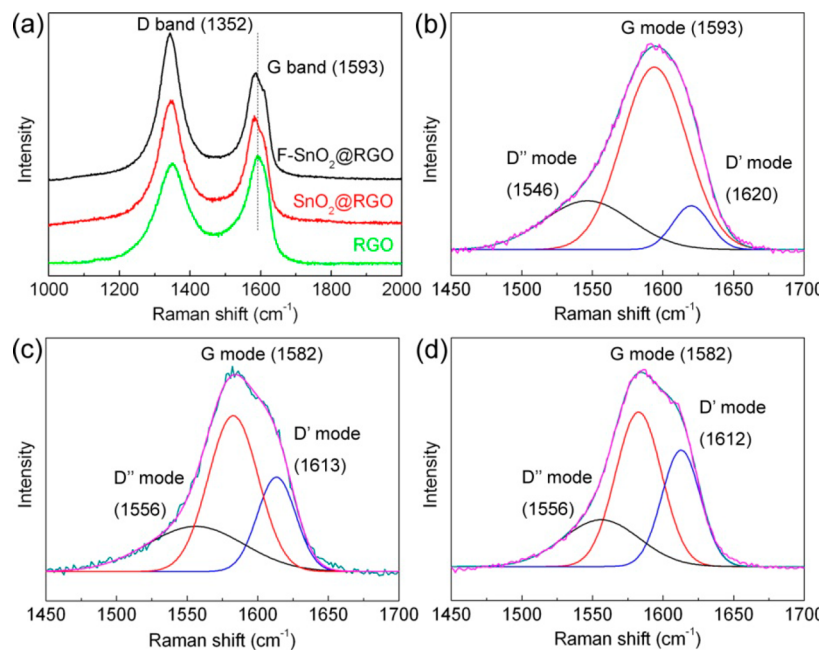


Figure 6. (a) Raman spectra of RGO, the SnO_2 @RGO and F-SnO_2 @RGO composites, showing the greater I_D/I_G ratios for the two composites than RGO. (b–d) Deconvoluted G-band of (b) RGO, (c) the SnO_2 @RGO composite, and (d) the F-SnO_2 @RGO composite, showing the low-frequency shifted G band of the two composites and the enhanced D' mode of the F-SnO_2 @RGO composite.

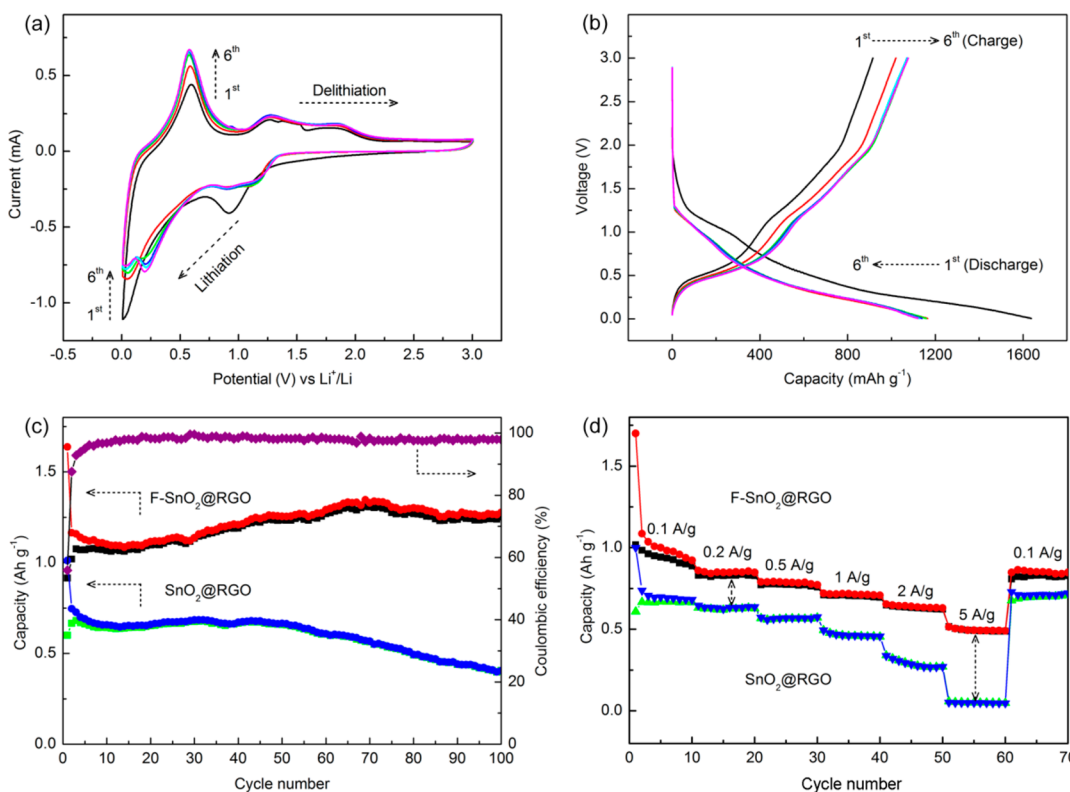


Figure 7. (a) First six cycles of the CV curves of the F-SnO_2 @RGO composite as anode material for LIBs. (b) First six cycles of the galvanostatic charge/discharge profiles. (c) Cycling performance of the F-SnO_2 @RGO and SnO_2 @RGO electrodes at a current density of 0.1 A g^{-1} and the Coulombic efficiency of the F-SnO_2 @RGO electrode, showing that the F-SnO_2 @RGO electrode exhibits a much higher capacity than the SnO_2 @RGO electrode. (d) Rate capability of the F-SnO_2 @RGO and SnO_2 @RGO electrodes, showing that the F-SnO_2 @RGO electrode exhibits better rate capacity than the SnO_2 @RGO electrode at a high charge/discharge current density.

SnO_2 nanoparticles and the RGO sheets, as discussed later. The uniform distribution of the F-SnO_2 nanoparticles on the RGO sheets can effectively prevent the $\text{Sn}/\text{F-SnO}_2$ nanoparticles

from sintering during the lithiation/delithiation cycles.¹⁸ Figure 5b, d displays the high-resolution TEM (HRTEM) images of the F-SnO_2 @RGO and SnO_2 @RGO composites. Lattice

fringes of (110) planes are commonly observed. The average size of the F-SnO₂ and the SnO₂ nanoparticles are calculated to be ca. 10 and 8 nm, in line with the results obtained from XRD data.

The interactions between the F-SnO₂ nanoparticles and RGO sheets were further investigated. Figure 6 show the Raman spectra of RGO and the SnO₂@RGO and F-SnO₂@RGO composites. It is seen that the two composites exhibit greater intensity ratios between the D-band (ca. 1352 cm⁻¹) and G-band (ca. 1593 cm⁻¹) of graphene (I_D/I_G) (1.14 and 1.38) than the RGO (0.93), implying a decreased average size of the sp² conjugated domains in the graphene sheets due to the presence of SnO₂ and F-SnO₂ nanoparticles.⁴⁰ Furthermore, the G bands of the SnO₂@RGO and F-SnO₂@RGO composites were also different from that of the RGO in position and shape. To gain a deeper understanding of the interfacial interactions in the composites, the G band was deconvoluted into three components: G mode, D' mode arising from the double resonance Raman process (at 1610–1620 cm⁻¹), and D'' mode originating from disorder induced first-order scattering (at 1550–1560 cm⁻¹) (Figure 6b–d).^{41,42} The G mode of the SnO₂@RGO and F-SnO₂@RGO composites shifted to a lower frequency (1582 cm⁻¹) compared with that of the RGO (1593 cm⁻¹). Such a low-frequency shift may be attributed to electron transfer from the SnO₂ and F-SnO₂ nanoparticles to the RGO sheets.^{43,44} In addition, the F-SnO₂@RGO composite generated a stronger D' mode than the SnO₂@RGO composites (Figure 6c, d). The stronger D' mode and the greater I_D/I_G ratio (Figure 6a) implied smaller sp² conjugated domains in the F-SnO₂@RGO composite than in the SnO₂@RGO composite. SnO₂ is an n-type semiconductor with a high free electron concentration due to the intrinsic defects.^{45,46} Electrons from SnO₂ flow into RGO in order for the Fermi level to become a constant through the system in thermal equilibrium. The Fermi level of F-SnO₂ is further elevated because of F doping, implying a higher free electron concentration in F-SnO₂.^{20,26} Therefore, more electrons would flow from the F-SnO₂ nanoparticles to RGO. As a result, the better developed 3D electron networks lead to further reduced size of sp²-conjugated domains in the F-SnO₂@RGO composite, and thereafter the interactions between the F-SnO₂ nanoparticles and the RGO sheets are stronger than that between the SnO₂ nanoparticles and the RGO sheets. In addition, the stronger interactions between F-SnO₂ nanoparticles and RGO sheets are also supported by the higher content of the F-SnO₂ nanoparticles attached on RGO sheets than that of SnO₂ nanoparticles (Figures S6 and S7 in the Supporting Information). As a result, the F-SnO₂ nanoparticles were more uniformly and densely decorated on the surface of RGO sheets than the SnO₂ nanoparticles (Figure 5a and Figure S5 in the Supporting Information). From the viewpoint of electrochemical process of LIBs, such uniform distribution of the F-SnO₂ nanoparticles would be beneficial to improving the performance of the LIB cells through alleviating the volume changes of the electrode material and the aggregation of the Sn particles during the lithiation/delithiation process.¹⁸

Next, efforts were directed toward testing the electrochemical performance of the F-SnO₂@RGO composite as an anode material for LIBs. Figure 7a and 7b show the first six cycles of the CV curves and the first six cycles of galvanostatic discharge/charge profiles, respectively. It is seen that a cathodic peak appeared at ca. 1 V in the first cathodic sweep process (Figure 7a), which led to a voltage plateau at ca. 1 V in the first

discharge profile (Figure 7b). This cathodic peak is attributed to the reduction of SnO₂ to Sn and the formation of solid-electrolyte interface.⁴⁷ Subsequently, one major and two minor peaks appeared at 0.60, 1.27, and 1.80 V in the first anodic sweep process. The major peak (at 0.60 V) was attributed to the delithiation process of Li_xSn species, while the two minor peaks (at 1.27 and 1.80 V) were related to the conversion of Sn into SnO₂.¹⁸ On the other hand, three corresponding cathodic peaks appeared at 0.19, 0.90, and 1.09 V in the second cathodic sweep process. Since the second cycle, the CV curves and the charge/discharge profiles are almost identical, indicating reversible and stable electrochemical performance of the F-SnO₂@RGO composite. Recently, H. Kim⁴⁸ observed the appearance of Sn–O bonds in the process of delithiation, which was ascribed to the reaction of Sn with the oxygen generated from the decomposition of Li₂O upon delithiation. Therefore, the conversion reaction of Sn to SnO₂ was turn out to be reversible. As a result, the F-SnO₂@RGO electrode delivered a discharge capacity of 1638 mA h g⁻¹ and a charge capacity of 915 mA h g⁻¹ calculated from the first discharge profile and the subsequent charge profile based on the total mass of the electrode material. A relatively high initial irreversible capacity loss can be identified, which could be ascribed to the formation of solid-electrolyte interface¹⁸ and additional contribution such as the reduction of SnO₂ to Sn.¹⁵

Figure 7c displays the cycling performance of the F-SnO₂@RGO electrode. After the first cycle, the discharge capacity dropped slightly, whereas the charge capacity increased, leading to a rapid increase of the Coulombic efficiency to a stable value that is close to 100%. Both the discharge and charge capacity of the F-SnO₂@RGO electrode started to increase gradually from the 14th cycle and reached a plateau at the 71th cycle (with a discharge capacity of 1339 mA h g⁻¹). After 100 charge/discharge cycles, the F-SnO₂@RGO electrode maintained a discharge capacity of 1277 mA h g⁻¹, which is ca. 3 times higher than the value for the SnO₂@RGO electrode in control experiments (405 mA h g⁻¹) and is one of the highest values among the SnO₂-based systems.^{2,16,17,47,49,50} The slightly higher content of F-SnO₂ in F-SnO₂@RGO composite than the SnO₂ in SnO₂@RGO composite (ca. 82 wt % for the former and ca. 75 wt % for the latter) might lead to a higher capacity of F-SnO₂@RGO electrode. However, the enhanced capacity of the F-SnO₂@RGO electrode should be mainly ascribed to F doping, since the three times enhancement in capacity of the F-SnO₂@RGO electrode is beyond the 7% increase of the F-SnO₂ nanoparticles in the F-SnO₂@RGO composite. Also, the F doping leads to improved cycling stability and better rate capacity at high charge/discharge current densities, as discussed later. The increase of the capacity during the initial cycles may be attributed to the improvement of ion accessibility in the hybrid, which leads to an increased accommodation behavior for Li.^{18,51} In control experiments, the SnO₂@RGO electrode showed not only a much lower specific capacity (Figure S8 in the Supporting Information and Figure 7c) than the F-SnO₂@RGO electrode but also a severe capacity fading. For the F-SnO₂@RGO composite, the high specific capacity was attributed to the chemical composition and the electrode structures, which led to a stable electrode with fast electron transportation, Li ion diffusion, and reduced electrochemical resistance in the cell. The stability of the F-SnO₂@RGO electrode can be derived from the corrosion resistant properties of F doping, which was reported to protect the electrode surface from the attack of HF produced from the hydrolysis or

decomposition of LiPF₆ and thereafter to result in stabilized structure of the resultant electrodes.^{23–25} In control experiments, compared with SnO₂ electrode, F-SnO₂ electrode without RGO also exhibits advantages in capacity and cycling stability (Figure S9a in the Supporting Information), which further prove the advantages of F doping including the corrosion-resistant properties.

In addition, the F-SnO₂@RGO electrode also exhibited highly reversible rate capacity, which was measured at current densities of 0.1, 0.2, 0.5, 1, 2, 5, and 0.1 A g⁻¹ (Figure 7d). Furthermore, the F-SnO₂@RGO electrode could maintain more specific capacity than the SnO₂@RGO electrode at a high current density, as one can see that the specific capacity of the F-SnO₂@RGO electrode dropped less than that of the SnO₂@RGO electrode as the charge/discharge current density increased (Figure 7d). This finding could be ascribed to the improved electrode kinetics of the F-SnO₂@RGO electrode. The improved electrode kinetics due to F doping are reflected in two aspects: (1) the enhanced electron transportation, which is caused by the increased electron carriers in the F-SnO₂ compared with in SnO₂, and (2) the improved Li ion diffusion because of the introduced defects and enlarged lattices,²³ which facilitate the insertion and diffusion of Li ions in the F-SnO₂@RGO electrode. As a result, the F-SnO₂@RGO electrode not only exhibits a much higher capacity than the SnO₂@RGO electrode at a high charge/discharge current density (634 mA h g⁻¹ for the former and 251 mA h g⁻¹ for the latter after 10 cycles at 5 A g⁻¹), but also shows excellent long-term cycling stability (464 mA h g⁻¹ for the former and 64 mA h g⁻¹ for the latter at 5 A g⁻¹ after 300 cycles) (Figure S10 in the Supporting Information). In control experiments, compared with SnO₂ electrode, the F-SnO₂ electrode without RGO also exhibited an enhanced rate capability (Figure S9b in the Supporting Information), further indicating the improved electrode kinetics due to F doping.

The superiority of the F-SnO₂@RGO electrode to the nondoped counterpart (SnO₂@RGO electrode) in electrode kinetics was further analyzed by EIS. Figure 8a shows the Nyquist plots of the F-SnO₂@RGO and SnO₂@RGO electrodes over a frequency range from 100 kHz to 10 mHz. The electrodes were measured at a fully charged state before and after the charge/discharge cycling test. The Nyquist plots could be well fit by using a commonly adopted equivalent circuit (the inset of Figure 8a),¹⁸ with the kinetic parameters summarized in Table S2 in the Supporting Information. The F-SnO₂@RGO electrode showed a lower film resistance (R_f) (70 Ω) than the SnO₂@RGO electrode (114 Ω) before the charge/discharge cycling test, due to the F doping of the electrode material. The electrical conductivity obtained from four-point probe measurement supported that the F-SnO₂@RGO composite had a higher electrical conductivity than the SnO₂@RGO composite (45 S cm⁻¹ for the former and 31 S cm⁻¹ for the latter). On the other hand, the F-SnO₂@RGO electrode also possessed a lower R_f (51.4 Ω) than the SnO₂@RGO electrode (55.1 Ω) after charge/discharge cycling test. This finding might indicate the integrity of the electrode structure due to the doped fluorine, which has protected the F-SnO₂@RGO electrode from corrosion by acidic species;²⁵ in return, this effect contributed to a stable long-term performance of the F-SnO₂@RGO electrode (Figure 7c and Figure S10 in the Supporting Information). Furthermore, the F-SnO₂@RGO electrode displayed smaller charge transfer resistance (R_{ct}) values than the SnO₂@RGO electrode for both before and after charge/

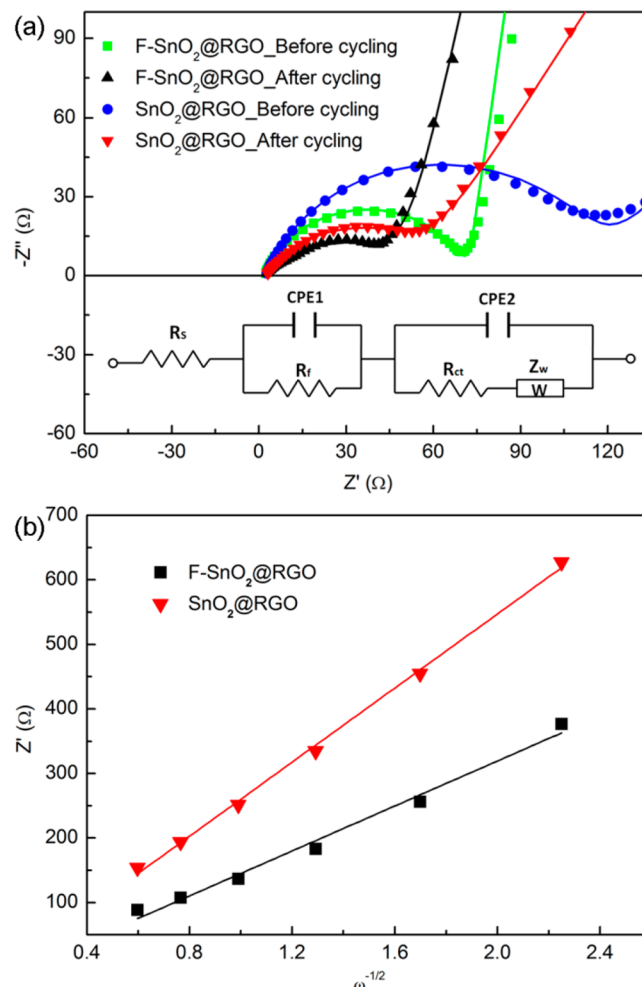


Figure 8. (a) Nyquist plots (solid dots) of the F-SnO₂@RGO and SnO₂@RGO electrodes measured at a fully charged state before and after charge/discharge cycling test and the fit curves (solid lines) using the equivalent circuit shown in the inset, showing that the F-SnO₂@RGO electrode exhibited semicircular arcs with shorter diameters than the SnO₂@RGO electrode. (b) The Z' – $\omega^{-1/2}$ plots for the F-SnO₂@RGO and SnO₂@RGO electrodes obtained after charge/discharge cycling test, indicating that the F-SnO₂@RGO electrode had a smaller σ value than the SnO₂@RGO electrode.

discharge cycling tests (Table S2 in the Supporting Information), indicating an enhanced charge transfer rate in the F-SnO₂@RGO electrode.⁵²

To elucidate the effect of F doping on Li ion diffusion in the electrode, we calculated Li ion diffusion coefficient (D_{Li}) from the Nyquist plots (Figure 8a) according to the following formulas:⁵³

$$Z' = R_{ct} + R_s + \sigma\omega^{-1/2} \quad (1)$$

$$D_{Li} = \frac{R^2 T^2}{2A^2 n^4 F^4 C_{Li}^2 \sigma^2} \quad (2)$$

where Z' is the real component of the impedance and has a linear relationship with $\omega^{-1/2}$ (ω , angular frequency); σ is the Warburg factor and obtained from the slope of the Z' – $\omega^{-1/2}$ line; and finally, D_{Li} is calculated by substituting the gas constant (R), the absolute temperature (T), electrode area (A), the number of electrons transferred in the half-reaction for the redox couple (n), the Faraday's constant (F), the concentration

of Li ions in solid (C_{Li} , 4.37×10^{-3} mol cm $^{-3}$), and σ .⁵⁴ Figure 8b displays the $Z' - \omega^{-1/2}$ plots of the F-SnO₂@RGO and SnO₂@RGO electrodes (after charge/discharge cycling test). One can see that the F-SnO₂@RGO electrode has a smaller σ than the SnO₂@RGO electrode (198 Ω rad $^{1/2}$ s $^{-1/2}$ for the former and 299 Ω rad $^{1/2}$ s $^{-1/2}$ for the latter). And then, the D_{Li} for the F-SnO₂@RGO electrode was calculated to be 9.87×10^{-17} cm 2 s $^{-1}$, which was two times greater than the value for the SnO₂@RGO electrode (4.32×10^{-17} cm 2 s $^{-1}$). Such values are comparable to the D_{Li} for other alloy- and conversion-type electrode materials.⁵⁵ This finding indicated that Li ions have a higher diffusion speed in the F-SnO₂@RGO electrode than in the SnO₂@RGO electrode. Copious experiments supported that such result was reproducible (Figure S11 in the Supporting Information).

CONCLUSIONS

In summary, for the first time, a composite of F-doped SnO₂ and RGO was synthesized by using Sn(BF₄)₂ as the single source of Sn and F through a hydrothermal process. XPS and XRD analysis indicated that the F atoms were doped in the unit cells of SnO₂. Raman spectra supported that the F-doped SnO₂ exhibited stronger interactions with the RGO sheets, leading to more uniform and denser decoration of the F-SnO₂ nanoparticles on the surfaces of the RGO sheets in the 3D architecture. Thanks to the aforementioned features, our F-SnO₂@RGO electrode exhibited remarkable properties such as fast access of electrolyte in the 3D structures, enhanced electron transportation and Li ion diffusion in the electrode due to F doping. As a result, the LIB cells prepared by using the F-SnO₂@RGO composite as anode material exhibited a specific capacity of 1277 mA h g $^{-1}$ after 100 cycles. In addition, the F-SnO₂@RGO electrode also displayed remarkable performance such as long-term cycling stability and excellent rate capacity at high charge/discharge current densities. And we expected that this work would narrow the gap between the basic research and the practical application of the SnO₂-based materials in LIBs.

ASSOCIATED CONTENT

Supporting Information

C 1s XPS curves of the F-SnO₂@RGO and SnO₂@RGO composites, SEM observations and EDS analysis of the F-SnO₂@RGO and SnO₂@RGO composites, N₂ adsorption–desorption isotherms of the SnO₂@RGO composite, TGA curves of the F-SnO₂@RGO and SnO₂@RGO composites, TEM observations of the F-SnO₂@RGO and SnO₂@RGO composites with different contents of nanoparticles, electrochemical characterization of the SnO₂@RGO composite, cycling performance and Nyquist plots of the F-SnO₂@RGO and SnO₂@RGO electrodes, electrochemical performance of F-SnO₂ and SnO₂ electrodes without RGO, and kinetic parameters of the F-SnO₂@RGO and SnO₂@RGO electrodes. The Supporting Information is available free of charge on the ACS Publications website at DOI: 10.1021/acs.chemmater.5b00885.

AUTHOR INFORMATION

Corresponding Author

*E-mail: jianxingeng@mail.ipc.ac.cn.

Notes

The authors declare no competing financial interest.

ACKNOWLEDGMENTS

This work was supported by the “Hundred Talents Program” of Chinese Academy of Sciences, the National Natural Science Foundation of China (U1362106).

REFERENCES

- Idota, Y.; Kubota, T.; Matsufuji, A.; Maekawa, Y.; Miyasaka, T. Tin-Based Amorphous Oxide: A High-Capacity Lithium-Ion-Storage Material. *Science* **1997**, *276*, 1395–1397.
- Zhou, X. S.; Dai, Z. H.; Liu, S. H.; Bao, J. C.; Guo, Y. G. Ultra-Uniform SnO_x/Carbon Nanohybrids toward Advanced Lithium-Ion Battery Anodes. *Adv. Mater.* **2014**, *26*, 3943–3949.
- Prabakar, S. J. R.; Hwang, Y. H.; Bae, E. G.; Shim, S.; Kim, D.; Lah, M. S.; Sohn, K. S.; Pyo, M. SnO₂/Graphene Composites with Self-Assembled Alternating Oxide and Amine Layers for High Li-Storage and Excellent Stability. *Adv. Mater.* **2013**, *25*, 3307–3312.
- Paek, S. M.; Yoo, E.; Honma, I. Enhanced Cyclic Performance and Lithium Storage Capacity of SnO₂/Graphene Nanoporous Electrodes with Three-Dimensionally Delaminated Flexible Structure. *Nano Lett.* **2009**, *9*, 72–75.
- Lee, S. H.; Mathews, M.; Toghiani, H.; Wipf, D. O.; Pittman, C. U., Jr. Fabrication of Carbon-Encapsulated Mono- and Bimetallic (Sn and Sn/Sb Alloy) Nanorods. Potential Lithium-Ion Battery Anode Materials. *Chem. Mater.* **2009**, *21*, 2306–2314.
- Kim, C.; Noh, M.; Choi, M.; Cho, J.; Park, B. Critical Size of a Nano SnO₂ Electrode for Li-Secondary Battery. *Chem. Mater.* **2005**, *17*, 3297–3301.
- Ding, S. J.; Chen, J. S.; Qi, G. G.; Duan, X. N.; Wang, Z. Y.; Giannelis, E. P.; Archer, L. A.; Lou, X. W. Formation of SnO₂ Hollow Nanospheres inside Mesoporous Silica Nanoreactors. *J. Am. Chem. Soc.* **2011**, *133*, 21–23.
- Wang, H. K.; Rogach, A. L. Hierarchical SnO₂ Nanostructures: Recent Advances in Design, Synthesis, and Applications. *Chem. Mater.* **2014**, *26*, 123–133.
- Sun, C. W.; Rajasekharan, S.; Goodenough, J. B.; Zhou, F. Monodisperse Porous LiFePO₄ Microspheres for a High Power Li-Ion Battery Cathode. *J. Am. Chem. Soc.* **2011**, *133*, 2132–2135.
- Luo, B.; Wang, B.; Liang, M. H.; Ning, J.; Li, X. L.; Zhi, L. J. Reduced Graphene Oxide-Mediated Growth of Uniform Tin-Core/Carbon-Sheath Coaxial Nanocables with Enhanced Lithium Ion Storage Properties. *Adv. Mater.* **2012**, *24*, 1405–1409.
- Lou, X. W.; Deng, D.; Lee, J. Y.; Archer, L. A. Preparation of SnO₂/Carbon Composite Hollow Spheres and Their Lithium Storage Properties. *Chem. Mater.* **2008**, *20*, 6562–6566.
- Chen, J. S.; Lou, X. W. SnO₂-Based Nanomaterials: Synthesis and Application in Lithium-Ion Batteries. *Small* **2013**, *9*, 1877–1893.
- Liang, J.; Yu, X. Y.; Zhou, H.; Wu, H. B.; Ding, S.; Lou, X. W. Bowl-Like SnO₂@Carbon Hollow Particles as an Advanced Anode Material for Lithium-Ion Batteries. *Angew. Chem., Int. Ed.* **2014**, *53*, 12803–12807.
- Lou, X. W.; Li, C. M.; Archer, L. A. Designed Synthesis of Coaxial SnO₂@Carbon Hollow Nanospheres for Highly Reversible Lithium Storage. *Adv. Mater.* **2009**, *21*, 2536–2539.
- Zhang, L.; Zhang, G. Q.; Wu, H. B.; Yu, L.; Lou, X. W. Hierarchical Tubular Structures Constructed by Carbon-Coated SnO₂ Nanoplates for Highly Reversible Lithium Storage. *Adv. Mater.* **2013**, *25*, 2589–2593.
- Lin, J.; Peng, Z. W.; Xiang, C. S.; Ruan, G. D.; Yan, Z.; Natelson, D.; Tour, J. M. Graphene Nanoribbon and Nanostructured SnO₂ Composite Anodes for Lithium Ion Batteries. *ACS Nano* **2013**, *7*, 6001–6006.
- Wang, X.; Cao, X. Q.; Bourgeois, L.; Guan, H.; Chen, S. M.; Zhong, Y. T.; Tang, D. M.; Li, H. Q.; Zhai, T. Y.; Li, L.; Bando, Y.; Golberg, D. N-Doped Graphene-SnO₂ Sandwich Paper for High-Performance Lithium-Ion Batteries. *Adv. Funct. Mater.* **2012**, *22*, 2682–2690.

- (18) Zhou, X. S.; Wan, L. J.; Guo, Y. G. Binding SnO₂ Nanocrystals in Nitrogen-Doped Graphene Sheets as Anode Materials for Lithium-Ion Batteries. *Adv. Mater.* **2013**, *25*, 2152–2157.
- (19) Wu, Z. S.; Ren, W. C.; Xu, L.; Li, F.; Cheng, H. M. Doped Graphene Sheets as Anode Materials with Superhigh Rate and Large Capacity for Lithium Ion Batteries. *ACS Nano* **2011**, *5*, 5463–5471.
- (20) Wang, Y. D.; Djerdj, I.; Smarsly, B.; Antonietti, M. Antimony-Doped SnO₂ Nanopowders with High Crystallinity for Lithium-Ion Battery Electrode. *Chem. Mater.* **2009**, *21*, 3202–3209.
- (21) Torabi, M.; Sadrnezhaad, S. K. Electrochemical Evaluation of Nanocrystalline Zn-Doped Tin Oxides as Anodes for Lithium Ion Microbatteries. *J. Power Sources* **2011**, *196*, 399–404.
- (22) Chopra, K. L.; Major, S.; Pandya, D. K. Transparent Conductors - A Status Review. *Thin Solid Films* **1983**, *102*, 1–46.
- (23) Woo, S. U.; Park, B. C.; Yoon, C. S.; Myung, S. T.; Prakash, J.; Sun, Y. K. Improvement of Electrochemical Performances of Li[Ni_{0.8}Co_{0.1}Mn_{0.1}]O₂ Cathode Materials by Fluorine Substitution. *J. Electrochem. Soc.* **2007**, *154*, A649–A655.
- (24) Jung, H. G.; Yoon, C. S.; Prakash, J.; Sun, Y. K. Mesoporous Anatase TiO₂ with High Surface Area and Controllable Pore Size by F⁻-Ion Doping: Applications for High-Power Li-ion Battery Anode. *J. Phys. Chem. C* **2009**, *113*, 21258–21263.
- (25) Ma, Y.; Ding, B.; Ji, G.; Lee, J. Y. Carbon-Encapsulated F-Doped Li₄Ti₅O₁₂ as a High Rate Anode Material for Li⁺ Batteries. *ACS Nano* **2013**, *7*, 10870–10878.
- (26) Gamard, A.; Babot, O.; Joussemae, B.; Rascle, M. C.; Toupancre, T.; Campet, G. Conductive F-Doped Tin Dioxide Sol-Gel Materials from Fluorinated Beta-Diketonate Tin(IV) Complexes. Characterization and Thermolytic Behavior. *Chem. Mater.* **2000**, *12*, 3419–3426.
- (27) Andersson, A.; Johansson, N.; Broms, P.; Yu, N.; Lupo, D.; Salaneck, W. R. Fluorine Tin Oxide as an Alternative to Indium Tin Oxide in Polymer LEDs. *Adv. Mater.* **1998**, *10*, 859–863.
- (28) Ha, H. W.; Kim, K.; de Borniol, M.; Toupancre, T. Fluorine-Doped Nanocrystalline SnO₂ Powders Prepared via a Single Molecular Precursor Method as Anode Materials for Li-Ion Batteries. *J. Solid State Chem.* **2006**, *179*, 702–707.
- (29) Hummers, W. S.; Offeman, R. E. Preparation of Graphitic Oxide. *J. Am. Chem. Soc.* **1958**, *80*, 1339–1339.
- (30) Geng, J. X.; Jung, H. Porphyrin Functionalized Graphene Sheets in Aqueous Suspensions: From the Preparation of Graphene Sheets to Highly Conductive Graphene Films. *J. Phys. Chem. C* **2010**, *114*, 8227–8234.
- (31) Cheng, G.; Wu, K.; Zhao, P. T.; Cheng, Y.; He, X. L.; Huang, K. X. Controlled Growth of Oxygen-Deficient Tin Oxide Nanostructures via a Solvothermal Approach in Mixed Solvents and Their Optical Properties. *Nanotechnology* **2007**, *18*, 355604.
- (32) Yang, H. G.; Zeng, H. C. Self-Construction of Hollow SnO₂ Octahedra Based on Two-Dimensional Aggregation of Nanocrystallites. *Angew. Chem., Int. Ed.* **2004**, *43*, 5930–5933.
- (33) Gong, Y. J.; Yang, S. B.; Zhan, L.; Ma, L. L.; Vajtai, R.; Ajayan, P. M. A Bottom-Up Approach to Build 3D Architectures from Nanosheets for Superior Lithium Storage. *Adv. Funct. Mater.* **2014**, *24*, 125–130.
- (34) Zhou, G. M.; Wang, D. W.; Yin, L. C.; Li, N.; Li, F.; Cheng, H. M. Oxygen Bridges between NiO Nanosheets and Graphene for Improvement of Lithium Storage. *ACS Nano* **2012**, *6*, 3214–3223.
- (35) Liang, Y. Y.; Wang, H. L.; Zhou, J. G.; Li, Y. G.; Wang, J.; Regier, T.; Dai, H. J. Covalent Hybrid of Spinel Manganese-Cobalt Oxide and Graphene as Advanced Oxygen Reduction Electrocatalysts. *J. Am. Chem. Soc.* **2012**, *134*, 3517–3523.
- (36) Li, H.; Fan, L.-Z. Effects of Fluorine Substitution on the Electrochemical Performance of Layered Li-Excess Nickel Manganese Oxides Cathode Materials for Lithium-Ion Batteries. *Electrochim. Acta* **2013**, *113*, 407–411.
- (37) Wang, Y. D.; Djerdj, I.; Antonietti, M.; Smarsly, B. Polymer-Assisted Generation of Antimony-Doped SnO₂ Nanoparticles with High Crystallinity for Application in Gas Sensors. *Small* **2008**, *4*, 1656–1660.
- (38) Shi, R.; Huang, G. L.; Lin, J.; Zhu, Y. F. Photocatalytic Activity Enhancement for Bi₂WO₆ by Fluorine Substitution. *J. Phys. Chem. C* **2009**, *113*, 19633–19638.
- (39) Memon, J.; Sun, J. H.; Meng, D. L.; Ouyang, W. Z.; Memon, M. A.; Huang, Y.; Yan, S. K.; Geng, J. X. Synthesis of Graphene/Ni-Al Layered Double Hydroxide Nanowires and Their Application as an Electrode Material for Supercapacitors. *J. Mater. Chem. A* **2014**, *2*, 5060–5067.
- (40) Huang, S.; Zhu, G. N.; Zhang, C.; Tjiu, W. W.; Xia, Y. Y.; Liu, T. X. Immobilization of Co-Al Layered Double Hydroxides on Graphene Oxide Nanosheets: Growth Mechanism and Supercapacitor Studies. *ACS Appl. Mater. Interfaces* **2012**, *4*, 2242–2249.
- (41) Mohiuddin, T. M. G.; Lombardo, A.; Nair, R. R.; Bonetti, A.; Savini, G.; Jalil, R.; Bonini, N.; Basko, D. M.; Gallois, C.; Marzari, N.; Novoselov, K. S.; Geim, A. K.; Ferrari, A. C. Uniaxial Strain in Graphene by Raman Spectroscopy: G Peak Splitting, Gruneisen Parameters, and Sample Orientation. *Phys. Rev. B* **2009**, *79*, 205433.
- (42) Ferrari, A. C.; Meyer, J. C.; Scardaci, V.; Casiraghi, C.; Lazzeri, M.; Mauri, F.; Piscanec, S.; Jiang, D.; Novoselov, K. S.; Roth, S.; Geim, A. K. Raman Spectrum of Graphene and Graphene Layers. *Phys. Rev. Lett.* **2006**, *97*, 187401.
- (43) Das, B.; Vogguru, R.; Rout, C. S.; Rao, C. N. R. Changes in the Electronic Structure and Properties of Graphene Induced by Molecular Charge-Transfer. *Chem. Commun.* **2008**, *41*, 5155–5157.
- (44) Geng, J.; Kong, B. S.; Yang, S. B.; Jung, H. T. Preparation of Graphene Relying on Porphyrin Exfoliation of Graphite. *Chem. Commun.* **2010**, *46*, 5091–5093.
- (45) Zhang, G. Z.; Xie, C. S.; Zhang, S. P.; Zhang, S. S.; Xiong, Y. Defect Chemistry of the Metal Cation Defects in the p- and n-Doped SnO₂ Nanocrystalline Films. *J. Phys. Chem. C* **2014**, *118*, 18097–18109.
- (46) Godinho, K. G.; Walsh, A.; Watson, G. W. Energetic and Electronic Structure Analysis of Intrinsic Defects in SnO₂. *J. Phys. Chem. C* **2009**, *113*, 439–448.
- (47) Li, X. F.; Meng, X. B.; Liu, J.; Geng, D. S.; Zhang, Y.; Banis, M. N.; Li, Y. L.; Yang, J. L.; Li, R. Y.; Sun, X. L.; Cai, M.; Verbrugge, M. W. Tin Oxide with Controlled Morphology and Crystallinity by Atomic Layer Deposition onto Graphene Nanosheets for Enhanced Lithium Storage. *Adv. Funct. Mater.* **2012**, *22*, 1647–1654.
- (48) Kim, H.; Park, G. O.; Kim, Y.; Muhammad, S.; Yoo, J.; Balasubramanian, M.; Cho, Y. H.; Kim, M. G.; Lee, B.; Kang, K.; Kim, H.; Kim, J. M.; Yoon, W. S. New Insight into the Reaction Mechanism for Exceptional Capacity of Ordered Mesoporous SnO₂ Electrodes via Synchrotron-Based X-Ray Analysis. *Chem. Mater.* **2014**, *26*, 6361–6370.
- (49) Wang, L.; Wang, D.; Dong, Z. H.; Zhang, F. X.; Jin, J. Interface Chemistry Engineering for Stable Cycling of Reduced GO/SnO₂ Nanocomposites for Lithium Ion Battery. *Nano Lett.* **2013**, *13*, 1711–1716.
- (50) Wang, D. N.; Yang, J. L.; Liu, J.; Li, X. F.; Li, R. Y.; Cai, M.; Sham, T. K.; Sun, X. L. Atomic Layer Deposited Coatings to Significantly Stabilize Anodes for Li Ion Batteries: Effects of Coating Thickness and the Size of Anode Particles. *J. Mater. Chem. A* **2014**, *2*, 2306–2312.
- (51) Wu, Z. S.; Sun, Y.; Tan, Y. Z.; Yang, S. B.; Feng, X. L.; Mullen, K. Three-Dimensional Graphene-Based Macro- and Mesoporous Frameworks for High-Performance Electrochemical Capacitive Energy Storage. *J. Am. Chem. Soc.* **2012**, *134*, 19532–19535.
- (52) Shu, K. W.; Wang, C. Y.; Wang, M.; Zhao, C.; Wallace, G. G. Graphene Cryogel Papers with Enhanced Mechanical Strength for High Performance Lithium Battery Anodes. *J. Mater. Chem. A* **2014**, *2*, 1325–1331.
- (53) Yi, T. F.; Xie, Y.; Wu, Q. J.; Liu, H. P.; Jiang, L. J.; Ye, M. F.; Zhu, R. S. High Rate Cycling Performance of Lanthanum-Modified Li₄Ti₅O₁₂ Anode Materials for Lithium-Ion Batteries. *J. Power Sources* **2012**, *214*, 220–226.
- (54) Faulkner, A. J. B. L. R. *Electrochemical Methods: Fundamentals and Applications*; Wiley: New York, 2001.

(55) Liu, B.; Zhao, X. Y.; Xiao, Y.; Cao, M. H. High-Surface-Area F-Doped Amorphous MoO_x with High-Performance Lithium Storage Properties. *J. Mater. Chem. A* **2014**, *2*, 3338–3343.